

A New Capability of E4D for 3D Parallel Joint Inversion of DC Resistivity and Traveltime Data on Unstructured Mesh

May 2020

Yue Zhu
Tim C. Johnson
Z. Fred Zhang

DISCLAIMER

This report was prepared as an account of work sponsored by an agency of the United States Government. Neither the United States Government nor any agency thereof, nor Battelle Memorial Institute, nor any of their employees, makes **any warranty, express or implied, or assumes any legal liability or responsibility for the accuracy, completeness, or usefulness of any information, apparatus, product, or process disclosed, or represents that its use would not infringe privately owned rights.** Reference herein to any specific commercial product, process, or service by trade name, trademark, manufacturer, or otherwise does not necessarily constitute or imply its endorsement, recommendation, or favoring by the United States Government or any agency thereof, or Battelle Memorial Institute. The views and opinions of authors expressed herein do not necessarily state or reflect those of the United States Government or any agency thereof.

PACIFIC NORTHWEST NATIONAL LABORATORY

operated by

BATTELLE

for the

UNITED STATES DEPARTMENT OF ENERGY

under Contract DE-AC05-76RL01830

Printed in the United States of America

Available to DOE and DOE contractors from the

Office of Scientific and Technical Information,

P.O. Box 62, Oak Ridge, TN 37831-0062;

ph: (865) 576-8401

fax: (865) 576-5728

email: reports@adonis.osti.gov

Available to the public from the National Technical Information Service

5301 Shawnee Rd., Alexandria, VA 22312

ph: (800) 553-NTIS (6847)

email: orders@ntis.gov <<https://www.ntis.gov/about>>

Online ordering: <http://www.ntis.gov>

A New Capability of E4D for 3D Parallel Joint Inversion of DC Resistivity and Traveltime Data on Unstructured Mesh

May 2020

Yue Zhu
Tim C. Johnson
Z. Fred Zhang

Prepared for
the U.S. Department of Energy
under Contract DE-AC05-76RL01830

Pacific Northwest National Laboratory
Richland, Washington 99354

Abstract

A major challenge in interpreting geophysical data is how to derive consistent three-dimensional (3D) earth models of different physical properties from spatially and temporally limited measurements. Joint inversion with cross-gradient constraints is an approach to find such models by imposing structural similarities between different physical parameters. We have developed a parallel distributed-memory joint inversion code for direct-current (DC) resistivity and traveltimes data using the cross-gradient constraint on unstructured mesh. The code utilizes existing E4D framework for parallel forward simulation, distributed storage and computation of the Jacobian matrix of forward operator, and parallel execution of matrix-vector multiplication during inversion. Besides, the joint inversion is solved by nonlinear conjugate gradient algorithm parallelized for DC resistivity and traveltimes data. The joint inversion capability of E4D was tested using synthetic data from cross-borehole DC resistivity and traveltimes data. The results indicate that the shape and size of the anomalies from the joint inversion are more reliable than those from separate inversions.

Acknowledgments

This study was supported by the Pacific Northwest National Laboratory's Laboratory-Directed Research & Development. The Pacific Northwest National Laboratory is operated by Battelle Memorial Institute for the DOE under Contract DE-AC05-76RL01830.

Acronyms and Abbreviations

3D	three-dimensional
DC	direct-current
NLCG	nonlinear conjugate gradient
PCG	preconditioned conjugate gradient
PIJI	preconditioned iterative joint inversion

Contents

Abstract.....	ii
Acknowledgments.....	iii
Acronyms and Abbreviations	iv
Contents	v
1.0 Introduction.....	1
2.0 Mathematical Formulations	2
2.1 Inverse equations	2
2.2 Parallel Inversion Algorithm	4
2.3 Gradient Calculation	6
3.0 Parallel Implementation	8
4.0 Synthetic Study	10
4.1 Synthetic Model Setup.....	10
4.2 Separate and Joint Inversion Results	11
4.3 Relationships Between Conductivity and Velocity	12
5.0 Conclusions.....	14
6.0 References.....	15

Figures

Figure 1. Generalized flow diagram demonstrating the (a) joint inversion process and (b) NLCG method. Gray box shows parallel tasks distributed among masters or slaves. Parallel computations of the forward simulation and Jacobian of the forward operator are distributed evenly among slaves and details can be found in Johnson et al. (2010).	8
Figure 2. Central computational domain and electrode positions. The travelttime receivers and transmitters are co-located with the electrodes. (a) Geometry of the two 8 m x 8 m x 5 m blocks. (b) Conductivity and velocity of the two blocks and surrounding area.....	10
Figure 3. Conductivity and velocity recovered from the separate and joint inversions. (a) Conductivity from the separate inversions. (b) Velocity from the separate inversions. (c) Conductivity from the joint inversion. (d) Velocity from the joint inversion.....	11
Figure 4. Cut-off plots of the recovered anomalies with background blanked off. The red rectangles indicate the true size and location of the two blocks. The shape and size of the anomalous conductivity and velocity are more correlated in the joint inversion results.	12
Figure 5. Cross plots of conductivity versus slowness (reverse of velocity) derived from the (a) separate and (b) joint inversions. Each dot represents an inversion element characterized by conductivity (x-axis) and slowness (y-axis). The blue and yellow dots represent the upper and lower anomalies and their surround areas, respectively.	13

1.0 Introduction

A variety of geophysical techniques are now available for non-intrusively interrogating the subsurface over large depth ranges (centimeters to kilometers) (Johnson et al. 2010; Lavoué et al. 2010; Martínez et al. 2010; Doolittle and Brevik 2014; Calamita et al. 2015; Johnson and Wellman 2015; Martini et al. 2017). As the sophistication of geophysical exploration increases, there are often several independent data sets available within a survey area. These data provide information about different physical properties of the subsurface. In many cases, this information is mutually complementary, making it natural to consider a joint inversion of different geophysical data for multiple physical properties. Moorkamp et al. (2011) summarized two reasons why joint inversion can narrow the set of acceptable models. First, different methods have complementary resolving kernels, which decreases the nonuniqueness of geophysical inversions. Second, the impact of noise differs for different geophysical methods so that adding another method improves the result more than adding data of the same type.

There are different approaches to recover multiple physical properties in a joint inversion. In the case where the corresponding model parameters are empirically or statistically correlated, the joint inversion can utilize the specific form of the correlation to reduce the number of unknowns (Jegen et al. 2009). This direct approach provides a strong coupling between the different model parameters and improves the inversion results when the given correlation is accurate. If the given correlation deviates away from the true relationship, one may get distorted or spurious imaging artifacts. An alternative method is to use the empirical or statistical correlation as a constraint, which provides a looser coupling compared to the direct approach and is less prone to erroneous results (Colombo and Stefano 2007).

However, in practical applications, the empirical or statistical correlation may exist, but its specific form may be unknown. In this case, the joint inversion can be based on structural-coupled constraints (Haber and Oldenburg 1997; Molodtsov et al. 2013). A commonly-used method is the cross-gradient approach (Gallardo and Meju 2004), which is based on minimizing a value of the cross-gradient function between different model parameters. Zhdanov et al. (2012) introduced another structural-coupled joint inversion approach using the Gramian constraints, which is computed as determinants of the corresponding Gram matrices of the multimodal model parameters or their different attributes. The Gramian constraint in the case of element-to-element structural coupling becomes identical to the cross-gradient function (Meju et al. 2019).

Structural-coupled joint inversion demands more computational resources than separate inversions. The computation and storage are doubled or tripled depending on how many physical properties are jointly inverted. In case of large-scale subsurface characterization and/or monitoring (time-lapse imaging), a parallel high-performance computing environment fits the joint inversion applications best. E4D is an open-source parallel geophysical modeling and inversion code with distributed-memory structure. It is beneficial to extend the existing E4D parallel capability for single geophysical methods, i.e., direct-current (DC) resistivity, spectral induced polarization, and travelt ime imaging, to the next stage of parallel joint inversion.

Here we discuss a parallel joint inversion code for DC resistivity and travelt ime data on unstructured mesh using the cross-gradient constraint. The objectives of this paper are to (1) outline numerical algorithm for solving the cross-gradient joint inversion on unstructured mesh, (2) develop parallel strategy for the joint inversion algorithm and implement it in the E4D (Johnson 2014), and (3) test the parallel joint inversion code using synthetic cross-borehole DC resistivity and travelt ime data. The development provides the capability of E4D of integrating large-scale data collected from multiple geophysical methods.

2.0 Mathematical Formulations

This section provides the mathematical formulations of the PIJI method with cross-gradient constraints that support the development of the joint inversion module for two different geophysical methods for unstructured mesh. The formulation can be extended to data from three or more geophysical methods. We first define the objective function for the joint inversion with cross-gradient constraints. The joint inversion is then translated to solving a system of linear equations with Taylor expansion of the nonlinear part of the objective function. After that, the PIJI method is presented to solve the linear system with two levels of iterations. Finally, numerical method to compute gradient on the unstructured tetrahedral mesh is derived in matrix notations.

2.1 Inverse equations

Consider a structural-coupled joint inversion of two model parameters $\mathbf{m}^{(1)}$ and $\mathbf{m}^{(2)}$, discretized on the same mesh, using the cross-gradient constraint. The structural-coupled joint inversion has the advantage over the direct-coupled method where explicit relationship between $\mathbf{m}^{(1)}$ and $\mathbf{m}^{(2)}$ is unknown or subject to large uncertainty. In the joint inversion we minimize the objective function (Φ_t), which is defined as the summation of data misfit (Φ_d), model misfit (Φ_m), and cross-gradient (Φ_{cg}) functions:

$$\Phi_t = \Phi_d + \Phi_m + \Phi_{cg} \quad (1)$$

where

$$\Phi_d = \sum_{i=1,2} \|\mathbf{W}_d^{(i)}(\mathbf{A}^{(i)}(\mathbf{m}^{(i)}) - \mathbf{d}_{obs}^{(i)})\|^2, \quad (1a)$$

$$\Phi_m = \sum_{i=1,2} \beta^{(i)} \|\mathbf{W}_m^{(i)}(\mathbf{m}^{(i)} - \mathbf{m}_{apr}^{(i)})\|^2, \quad (1b)$$

$$\Phi_{cg} = \beta_{cg} \|\vec{\boldsymbol{\tau}}(\mathbf{m}^{(1)}, \mathbf{m}^{(2)})\|^2, \quad (1b)$$

with data weighting matrices $\mathbf{W}_d^{(i)}$, nonlinear forward operators $\mathbf{A}^{(i)}$, observed data vectors $\mathbf{d}_{obs}^{(i)}$, regularization parameters $\beta^{(i)}$, model weighting matrices $\mathbf{W}_m^{(i)}$, a priori model vectors $\mathbf{m}_{apr}^{(i)}$, structural coupling parameter β_{cg} , and cross-gradient function $\vec{\boldsymbol{\tau}}(\mathbf{m}^{(1)}, \mathbf{m}^{(2)})$, for $i = 1$ and 2 .

The cross-gradient function $\vec{\boldsymbol{\tau}}(\mathbf{m}^{(1)}, \mathbf{m}^{(2)})$ in Eq. (1c) is a nonlinear vector function of $\mathbf{m}^{(1)}$ and $\mathbf{m}^{(2)}$, defined as the cross product of two gradient vectors

$$\vec{\boldsymbol{\tau}}(\mathbf{m}^{(1)}, \mathbf{m}^{(2)}) = \nabla \mathbf{m}^{(1)} \times \nabla \mathbf{m}^{(2)}. \quad (2)$$

The vector function $\vec{\boldsymbol{\tau}}(\mathbf{m}^{(1)}, \mathbf{m}^{(2)})$ provides element-to-element measurement of the structural differences between $\mathbf{m}^{(1)}$ and $\mathbf{m}^{(2)}$. Smaller magnitude of $\vec{\boldsymbol{\tau}}(\mathbf{m}^{(1)}, \mathbf{m}^{(2)})$ means more similar structure between $\mathbf{m}^{(1)}$ and $\mathbf{m}^{(2)}$. Scalar components of $\vec{\boldsymbol{\tau}}(\mathbf{m}^{(1)}, \mathbf{m}^{(2)})$ are computed as

$$\tau_x = (\partial_y \mathbf{m}^{(1)})(\partial_z \mathbf{m}^{(2)}) - (\partial_z \mathbf{m}^{(1)})(\partial_y \mathbf{m}^{(2)}), \quad (3)$$

$$\tau_y = (\partial_z \mathbf{m}^{(1)})(\partial_x \mathbf{m}^{(2)}) - (\partial_x \mathbf{m}^{(1)})(\partial_z \mathbf{m}^{(2)}), \quad (4)$$

$$\tau_z = (\partial_x \mathbf{m}^{(1)})(\partial_y \mathbf{m}^{(2)}) - (\partial_y \mathbf{m}^{(1)})(\partial_x \mathbf{m}^{(2)}). \quad (5)$$

For the case with data from three or more geophysical methods, the data sets need to be paired up and the cross-gradient function for each pair is calculated.

Localized linearization of the nonlinear functions $\mathbf{A}^{(i)}(\mathbf{m}^{(i)})$ and $\vec{\tau}(\mathbf{m}^{(1)}, \mathbf{m}^{(2)})$ are needed for solving the optimization problem Eq. (1). Given starting models $\mathbf{m}_0^{(i)}$, $\mathbf{A}^{(i)}(\mathbf{m}^{(i)})$ and $\vec{\tau}(\mathbf{m}^{(1)}, \mathbf{m}^{(2)})$ can be approximated using a first-order Taylor expansion as

$$\mathbf{A}^{(i)}(\mathbf{m}^{(i)}) \approx \mathbf{A}^{(i)}(\mathbf{m}_0^{(i)}) + \mathbf{J}^{(i)}\Delta\mathbf{m}^{(i)}, i = 1, 2, \quad (6)$$

$$\vec{\tau}(\mathbf{m}^{(1)}, \mathbf{m}^{(2)}) \approx \vec{\tau}(\mathbf{m}_0^{(1)}, \mathbf{m}_0^{(2)}) + \mathbf{B}^{(1)}\Delta\mathbf{m}^{(1)} + \mathbf{B}^{(2)}\Delta\mathbf{m}^{(2)}. \quad (7)$$

where $\mathbf{J}^{(i)}$ and $\mathbf{B}^{(i)}$ are the Jacobian matrices (i.e. first order partial derivatives) of $\mathbf{A}^{(i)}(\mathbf{m}^{(i)})$ and $\vec{\tau}(\mathbf{m}^{(1)}, \mathbf{m}^{(2)})$ with respect to $\mathbf{m}^{(i)}$. Details concerning computations of $\mathbf{J}^{(i)}$ are beyond the scope of this paper but can be found in manuscripts addressing separate geophysical inversions (Johnson et al. 2010; Lelièvre et al. 2011). Matrices $\mathbf{B}^{(i)}$ are computed as

$$\mathbf{B}^{(1)} = \begin{bmatrix} \text{diag}(\mathbf{D}_z \mathbf{m}_0^{(2)})\mathbf{D}_y - \text{diag}(\mathbf{D}_y \mathbf{m}_0^{(2)})\mathbf{D}_z \\ \text{diag}(\mathbf{D}_x \mathbf{m}_0^{(2)})\mathbf{D}_z - \text{diag}(\mathbf{D}_z \mathbf{m}_0^{(2)})\mathbf{D}_x \\ \text{diag}(\mathbf{D}_y \mathbf{m}_0^{(2)})\mathbf{D}_x - \text{diag}(\mathbf{D}_x \mathbf{m}_0^{(2)})\mathbf{D}_y \end{bmatrix}, \quad (8)$$

and

$$\mathbf{B}^{(2)} = \begin{bmatrix} \text{diag}(\mathbf{D}_y \mathbf{m}_0^{(1)})\mathbf{D}_z - \text{diag}(\mathbf{D}_z \mathbf{m}_0^{(1)})\mathbf{D}_y \\ \text{diag}(\mathbf{D}_z \mathbf{m}_0^{(1)})\mathbf{D}_x - \text{diag}(\mathbf{D}_x \mathbf{m}_0^{(1)})\mathbf{D}_z \\ \text{diag}(\mathbf{D}_x \mathbf{m}_0^{(1)})\mathbf{D}_y - \text{diag}(\mathbf{D}_y \mathbf{m}_0^{(1)})\mathbf{D}_x \end{bmatrix}, \quad (9)$$

where $\text{diag}(\mathbf{v})$ returns a diagonal matrix with the elements of vector \mathbf{v} on the main diagonal. The matrices \mathbf{D}_x , \mathbf{D}_y and \mathbf{D}_z are discrete forms of differential operators ∂_x , ∂_y , and ∂_z on a general unstructured mesh. Note that the matrices $\mathbf{B}^{(1)}$ and $\mathbf{B}^{(2)}$ share the same sparsity pattern of the discrete differential operators.

Substituting Eq. **Error! Reference source not found.** and **Error! Reference source not found.** into Eq. (1a) and (1c) results the linearized objective function

$$\Phi_t = \tilde{\Phi}_d + \Phi_{cg}, \quad (10)$$

where

$$\tilde{\Phi}_d = \Phi_d + \Phi_m = \sum_{i=1,2} \|\tilde{\mathbf{J}}^{(i)}\Delta\mathbf{m}^{(i)} + \tilde{\mathbf{A}}^{(i)}(\mathbf{m}_0^{(i)}) - \mathbf{b}^{(i)}\|^2,$$

**Error!
Reference
source
not
found.a)**

$$\Phi_{cg} = \beta_{cg} \|\mathbf{B}^{(1)}\Delta\mathbf{m}^{(1)} + \mathbf{B}^{(2)}\Delta\mathbf{m}^{(2)} + \vec{\tau}(\mathbf{m}_0^{(1)}, \mathbf{m}_0^{(2)})\|^2.$$

**Error!
Reference
source
not
found.b)**

with $\tilde{\mathbf{J}}^{(i)} = \left[\frac{\mathbf{W}_d^{(i)} \mathbf{J}^{(i)}}{\sqrt{\beta^{(i)}} \mathbf{W}_m^{(i)}} \right]$, $\tilde{\mathbf{A}}^{(i)}(\mathbf{m}_0^{(i)}) = \left[\frac{\mathbf{W}_d^{(i)} \mathbf{A}^{(i)}(\mathbf{m}_0^{(i)})}{\sqrt{\beta^{(i)}} \mathbf{W}_m^{(i)} \mathbf{m}_0^{(i)}} \right]$, and $\mathbf{b}^{(i)} = \left[\frac{\mathbf{W}_d^{(i)} \mathbf{d}_{obs}^{(i)}}{\sqrt{\beta^{(i)}} \mathbf{W}_m^{(i)} \mathbf{m}_{appr}^{(i)}} \right]$, for $i = 1$ and

2. Eq. **Error! Reference source not found.** merges the data and model misfit functions (Φ_d and Φ_m) into one generalized data misfit function $\tilde{\Phi}_d$ for shorter expressions.

Minimizing Eq. **Error! Reference source not found.** leads to solving the following linear system for $\Delta\mathbf{m}$

$$\mathbf{H}\Delta\mathbf{m} = \mathbf{s} \quad (11)$$

where \mathbf{H} is a symmetric positive-definite matrix

$$\mathbf{H} = \begin{bmatrix} \tilde{\mathbf{J}}^{(1)\text{T}}\tilde{\mathbf{J}}^{(1)} + \beta_{cg}\mathbf{B}^{(1)\text{T}}\mathbf{B}^{(1)} & \beta_{cg}\mathbf{B}^{(1)\text{T}}\mathbf{B}^{(2)} \\ \beta_{cg}\mathbf{B}^{(2)\text{T}}\mathbf{B}^{(1)} & \tilde{\mathbf{J}}^{(2)\text{T}}\tilde{\mathbf{J}}^{(2)} + \beta_{cg}\mathbf{B}^{(2)\text{T}}\mathbf{B}^{(2)} \end{bmatrix}, \quad (12)$$

and \mathbf{s} is the right-hand side vector

$$\mathbf{s} = \begin{bmatrix} \tilde{\mathbf{J}}^{(1)\text{T}}(\tilde{\mathbf{b}}^{(1)} - \tilde{\mathbf{A}}^{(i)}(\mathbf{m}_0^{(1)})) - \beta_{cg}\mathbf{B}^{(1)\text{T}}\tilde{\boldsymbol{\tau}}(\mathbf{m}_0^{(1)}, \mathbf{m}_0^{(2)}) \\ \tilde{\mathbf{J}}^{(2)\text{T}}(\tilde{\mathbf{b}}^{(2)} - \tilde{\mathbf{A}}^{(i)}(\mathbf{m}_0^{(2)})) - \beta_{cg}\mathbf{B}^{(2)\text{T}}\tilde{\boldsymbol{\tau}}(\mathbf{m}_0^{(1)}, \mathbf{m}_0^{(2)}) \end{bmatrix}. \quad (13)$$

From now on, we arrange vectors $\Delta\mathbf{m}^{(1)}$ and $\Delta\mathbf{m}^{(2)}$ into one big vector $\Delta\mathbf{m} = \begin{bmatrix} \Delta\mathbf{m}^{(1)} \\ \Delta\mathbf{m}^{(2)} \end{bmatrix}$ for convenience, similarly for \mathbf{m}_0 , \mathbf{d}_{obs} , $\mathbf{A}(\mathbf{m}_0)$, etc.

The preconditioned conjugate gradient (PCG) algorithm is used in this paper to solve the linear system Eq. **Error! Reference source not found.** (Shewchuk 1994; Ascher and Greif 2011). Although $\mathbf{W}_d^{(i)}$, $\mathbf{W}_m^{(i)}$, and $\mathbf{B}^{(i)}$ are sparse with small storage requirements, $\mathbf{J}^{(i)}$ and hence \mathbf{H} matrices are large and dense. As a result, iterative gradient-type algorithms (e.g. conjugate gradient) are more feasible than direct solvers (e.g. Cholesky or QR) for Eq. **Error! Reference source not found.** in terms of computational cost and especially the memory requirement for large 3D inversion problems. A Jacobi preconditioner (i.e. diagonal of \mathbf{H}) is suggested to use for scaling the different units/magnitudes of $\mathbf{m}^{(1)}$ and $\mathbf{m}^{(2)}$.

2.2 Parallel Inversion Algorithm

The nonlinearity of the objective function in Eq. (1) requires to iteratively formulate and solve the linear system Eq. **Error! Reference source not found.** using the PCG algorithm. That is, linearize the objective function in Eq. (1) at starting model \mathbf{m}_0 towards Eq. **Error! Reference source not found.**, solve the linear system Eq. **Error! Reference source not found.** for $\Delta\mathbf{m}$, add $\Delta\mathbf{m}$ to \mathbf{m}_0 for new starting model \mathbf{m}_1 , and repeat this process until the observed data are matched to within some criteria determined by the data noise. This joint inversion process therefore has two levels (i.e. outer and inner) of iterations. The outer iteration updates \mathbf{H} and \mathbf{s} in Eq. **Error! Reference source not found.** and **Error! Reference source not found.** and the inner iteration solves Eq. **Error! Reference source not found.** using the PCG algorithm. For computational efficiency, we do not explicitly formulate the \mathbf{H} and \mathbf{s} but break the \mathbf{H} -related computation of $\mathbf{H}\mathbf{x}$ into smaller matrix-vector multiplications involving $\tilde{\mathbf{J}}^{(i)}$, $\tilde{\mathbf{J}}^{(i)\text{T}}$, $\mathbf{B}^{(i)}$, and $\mathbf{B}^{(i)\text{T}}$, and split \mathbf{s} into two smaller vectors $\mathbf{s}^{(1)}$ and $\mathbf{s}^{(2)}$. That is,

$$\mathbf{H}\mathbf{x} = \begin{bmatrix} \tilde{\mathbf{J}}^{(1)\text{T}} & \mathbf{0} & \mathbf{B}^{(1)\text{T}} \\ \mathbf{0} & \tilde{\mathbf{J}}^{(2)\text{T}} & \mathbf{B}^{(2)\text{T}} \end{bmatrix} \begin{bmatrix} \tilde{\mathbf{J}}^{(1)} & \mathbf{0} \\ \mathbf{0} & \tilde{\mathbf{J}}^{(2)} \\ \mathbf{B}^{(1)} & \mathbf{B}^{(2)} \end{bmatrix} \begin{bmatrix} \mathbf{x}^{(1)} \\ \mathbf{x}^{(2)} \end{bmatrix} \text{ and } \mathbf{s} = \begin{bmatrix} \mathbf{s}^{(1)} \\ \mathbf{s}^{(2)} \end{bmatrix} \quad (14)$$

Assuming $\tilde{\mathbf{J}}^{(i)}$, $\mathbf{B}^{(i)}$, $\tilde{\mathbf{b}}^{(i)}$, $\tilde{\mathbf{A}}^{(i)}(\mathbf{m}_k^{(i)})$, and $\tilde{\boldsymbol{\tau}}(\mathbf{m}_k^{(1)}, \mathbf{m}_k^{(2)})$, $i = 1, 2$, have been computed, the PCG algorithm (inner iterations of the joint inversion process) can be expressed by the following operations in equations (15)-(35).

$$\mathbf{r}^{(i)} = \tilde{\mathbf{b}}^{(i)} - \tilde{\mathbf{A}}^{(i)}(\mathbf{m}_k^{(i)}), i = 1, 2 \quad (15)$$

$$\mathbf{v} = -\tilde{\boldsymbol{\tau}}(\mathbf{m}_k^{(1)}, \mathbf{m}_k^{(2)}) \quad (16)$$

$$\mathbf{s}^{(i)} = \tilde{\mathbf{J}}^{(i)\text{T}}\mathbf{r}^{(i)} + \beta_{cg}\mathbf{B}^{(i)\text{T}}\mathbf{v}, i = 1, 2 \quad (17)$$

$$\mathbf{h}^{(i)} = (\mathbf{P}^{(i)})^{-1}\mathbf{s}^{(i)}, i = 1, 2 \quad (18)$$

$$\mathbf{p}^{(i)} = \mathbf{h}^{(i)}, i = 1, 2 \quad (19)$$

$$\gamma = \sum_i \mathbf{s}^{(i)\text{T}}\mathbf{h}^{(i)} \quad (20)$$

$$N_0 = \gamma^{1/2} \quad (21)$$

$$\Delta \mathbf{m}^{(i)} = \mathbf{0}, i = 1, 2 \quad (22)$$

start loop

$$\mathbf{q}^{(i)} = \check{\mathbf{J}}^{(i)} \mathbf{p}^{(i)}, i = 1, 2 \quad (23)$$

$$\delta = \Sigma_i \mathbf{q}^{(i)T} \mathbf{q}^{(i)} \quad (24)$$

$$\mathbf{u} = \Sigma_i \mathbf{B}^{(i)} \mathbf{p}^{(i)} \quad (25)$$

$$\alpha = \gamma / (\delta + \beta_{cg} \mathbf{u}^T \mathbf{u}) \quad (26)$$

$$\Delta \mathbf{m}^{(i)} = \alpha \mathbf{p}^{(i)}, i = 1, 2 \quad (27)$$

$$\mathbf{r}^{(i)} = \mathbf{r}^{(i)} - \alpha \mathbf{q}^{(i)}, i = 1, 2 \quad (28)$$

$$\mathbf{v} = \mathbf{v} - \alpha \mathbf{u} \quad (29)$$

$$\mathbf{s}^{(i)} = \check{\mathbf{J}}^{(i)T} \mathbf{r}^{(i)} + \beta_{cg} \mathbf{B}^{(i)T} \mathbf{v}, i = 1, 2 \quad (30)$$

$$\mathbf{h}^{(i)} = (\mathbf{P}^{(i)})^{-1} \mathbf{s}^{(i)}, i = 1, 2 \quad (31)$$

$$\gamma_1 = \gamma \quad (32)$$

$$\gamma = \Sigma_i \mathbf{s}^{(i)T} \mathbf{h}^{(i)} \quad (33)$$

$$N = \gamma^{1/2} \quad (34)$$

$$\mathbf{p}^{(i)} = \mathbf{h}^{(i)} + \gamma / \gamma_1 \mathbf{p}^{(i)}, i = 1, 2 \quad (35)$$

if convergence criteria satisfied then exit loop

end loop

The PCG or inner iteration convergence criteria referenced after equation (35) typically is based upon the magnitude of the decrease in N with respect to N_0 between iterations or until some user-specified maximum number is reached. Each of equations (15) to (35) can be computed independently for physics 1 (i.e. DC resistivity) and physics 2 (i.e. travelttime) except equations (20), (24), (25), and (33). Consequently, we conduct the joint inversion by two main parallel processes. One is executed by master processor 0 and slave processors 1 to n ; the other is executed by master processor 1 and slave processors $n + 1$ to $n + m$. The number of slave processors n for physics 1 and m for physics 2 are determined by users. Master processors 0 and 1 compute equations (15) through (35) independently in parallel except equations (20), (24), (25), and (33), where communications between the two physics through master processors are involved. In addition, the matrix-vector multiplications involving $\check{\mathbf{J}}^{(i)}$ and $\check{\mathbf{J}}^{(i)T}$ in equations (17), (23), and (30) are computed on slave processors for each physics. Johnson et al. (2010) has full description about the distributed parallel computations of $\check{\mathbf{J}}^{(i)} \mathbf{p}^{(i)}$ and $\check{\mathbf{J}}^{(i)T} \mathbf{r}^{(i)}$. (To mention that, all communications between the two physics are managed by master processors only. That is, there is no communication of slave processors between different physics.)

Solution to the joint inversion is subject to the initial model \mathbf{m}_0 because of possible local minima associated with Eq. (1). To make best guess of \mathbf{m}_0 , β_{cg} is set to zero in the first few outer iterations until the data misfit Φ_d drops to certain user specified value. This strategy is equivalent to using an initial model \mathbf{m}_0 close to results obtained from separate inversions. During the iterative inversion process, parameters $\beta^{(i)}$ and β_{cg} are adjusted to provide solutions that maintain the data fit but also maximize the model constraints and structural similarities between $\mathbf{m}^{(1)}$ and $\mathbf{m}^{(2)}$ to the extent possible.

The matrix \mathbf{H} in Eq. **Error! Reference source not found.** can be written as the sum of two matrices as

$$\mathbf{H} = \mathbf{H}_p + \mathbf{H}_s, \quad (36)$$

where

$$\mathbf{H}_p = \begin{bmatrix} \tilde{\mathbf{j}}^{(1)\text{T}}\tilde{\mathbf{j}}^{(1)} + \beta_{cg}\mathbf{B}^{(1)\text{T}}\mathbf{B}^{(1)} & \mathbf{0} \\ \mathbf{0} & \tilde{\mathbf{j}}^{(2)\text{T}}\tilde{\mathbf{j}}^{(2)} + \beta_{cg}\mathbf{B}^{(2)\text{T}}\mathbf{B}^{(2)} \end{bmatrix},$$

Error!
Reference
source
not
found.a)

$$\mathbf{H}_s = \begin{bmatrix} \mathbf{0} & \beta_{cg}\mathbf{B}^{(1)\text{T}}\mathbf{B}^{(2)} \\ \beta_{cg}\mathbf{B}^{(2)\text{T}}\mathbf{B}^{(1)} & \mathbf{0} \end{bmatrix}.$$

Error!
Reference
source
not
found.b)

The \mathbf{H}_p (principal \mathbf{H}) and \mathbf{H}_s (secondary \mathbf{H}) are related to the non-mixed and mixed second-order derivatives of Φ_t . In the NLCG method, one can use the exact \mathbf{H} matrix, or approximate it with \mathbf{H}_p by dropping the term \mathbf{H}_s . Note that, the linear system Eq. **Error! Reference source not found.** becomes easier to solve by replacing \mathbf{H} with \mathbf{H}_p because it can break down into two smaller linear systems. As a result, the coding effort for the NLCG method using \mathbf{H}_p is smaller than \mathbf{H} .

In our PCG algorithm, we use the full \mathbf{H} matrix. It's also fine to drop the H_s part and approximate H by H_p . The benefits of doing so are (1) The matrix-inverse can now be divided into two smaller linear systems (put equations here), which may suit for some specific software framework, and (2) communication between the two physics can be limited to the outer iteration of the inversion, which may save communication time/coding effort where communication/coding overhead is a big concern.

2.3 Gradient Calculation

Gradients are necessary for computing the cross-gradient function in the joint inversion, more specifically constructing the matrices $\mathbf{B}^{(i)}$ in Eq. **Error! Reference source not found.** and **Error! Reference source not found.**. For structured orthogonal grids, the gradient can be easily computed using the standard finite difference approximations (i.e. forward, backward, and central differences). The case becomes more complicated when general unstructured mesh is involved, for example the tetrahedral cells that are used by E4D. Typical methods to evaluate the gradient ∇m of a given scalar m include the Green-Gauss method and the least squares method. The Green-Gauss method is an intuitive, explicit method to compute gradient that utilizes the Green-Gauss theorem. For unstructured meshes, the accuracy of this method decreases with increasing irregularity of the cells. In this case, the least squares method can be used for accurate evaluation of the gradient, although it is an implicit method requiring matrix inversion.

Consider a tetrahedral cell with centroid \mathbf{c}_0 and four neighboring cells with centroid $\mathbf{c}_i, i = 1,4$. The change in m between \mathbf{c}_0 and \mathbf{c}_i is assumed to vary linearly along the vector $\Delta\mathbf{c}_i = \mathbf{c}_i - \mathbf{c}_0$ as

$$(\nabla m)_{c_0} \cdot \Delta\mathbf{c}_i = (m_{c_i} - m_{c_0}), i = 1,4 \quad (37)$$

Eq. **Error! Reference source not found.** can be arranged into the following linear system in compact form

$$\mathbf{C} \begin{bmatrix} (\partial_x m)_{c_0} \\ (\partial_y m)_{c_0} \\ (\partial_z m)_{c_0} \end{bmatrix} = \mathbf{L} \begin{bmatrix} m_{c_0} \\ m_{c_1} \\ m_{c_2} \\ m_{c_3} \\ m_{c_4} \end{bmatrix}, \quad (38)$$

where \mathbf{C} is a 4×3 coefficient matrix which is purely a function of geometry

$$\mathbf{C} = \begin{bmatrix} x_{c_1} - x_{c_0} & y_{c_1} - y_{c_0} & z_{c_1} - z_{c_0} \\ x_{c_2} - x_{c_0} & y_{c_2} - y_{c_0} & z_{c_2} - z_{c_0} \\ x_{c_3} - x_{c_0} & y_{c_3} - y_{c_0} & z_{c_3} - z_{c_0} \\ x_{c_4} - x_{c_0} & y_{c_4} - y_{c_0} & z_{c_4} - z_{c_0} \end{bmatrix}, \quad (39)$$

and \mathbf{L} is a 4×5 constant matrix

$$\mathbf{L} = \begin{bmatrix} -1 & 1 & & & \\ -1 & & 1 & & \\ -1 & & & 1 & \\ -1 & & & & 1 \end{bmatrix}. \quad (40)$$

Eq. **Error! Reference source not found.** is an over-determined linear system. Its least squares solution is given by

$$\begin{bmatrix} (\partial_x m)_{c_0} \\ (\partial_y m)_{c_0} \\ (\partial_z m)_{c_0} \end{bmatrix} = (\mathbf{C}^T \mathbf{C})^{-1} \mathbf{C}^T \mathbf{L} \begin{bmatrix} m_{c_0} \\ m_{c_1} \\ m_{c_2} \\ m_{c_3} \\ m_{c_4} \end{bmatrix}, \quad (41)$$

where the 3×3 matrix inverse $(\mathbf{C}^T \mathbf{C})^{-1}$ can be efficiently computed due to its small size. Denoting the rows of the 3×5 matrix $(\mathbf{C}^T \mathbf{C})^{-1} \mathbf{C}^T \mathbf{L}$ with row vectors $(\mathbf{D}_x)_{c_0}$, $(\mathbf{D}_y)_{c_0}$, and $(\mathbf{D}_z)_{c_0}$, Eq. **Error! Reference source not found.** can be rewritten as

$$\begin{bmatrix} (\partial_x m)_{c_0} \\ (\partial_y m)_{c_0} \\ (\partial_z m)_{c_0} \end{bmatrix} = \begin{bmatrix} (\mathbf{D}_x)_{c_0} \\ (\mathbf{D}_y)_{c_0} \\ (\mathbf{D}_z)_{c_0} \end{bmatrix} \begin{bmatrix} m_{c_0} \\ m_{c_1} \\ m_{c_2} \\ m_{c_3} \\ m_{c_4} \end{bmatrix}, \quad (42)$$

Eq. **Error! Reference source not found.** is then assembled into a larger linear system by computing $(\mathbf{D}_x)_{c_0}$, $(\mathbf{D}_y)_{c_0}$, and $(\mathbf{D}_z)_{c_0}$, for every cell of the mesh, resulting

$$\begin{bmatrix} \partial_x \mathbf{m} \\ \partial_y \mathbf{m} \\ \partial_z \mathbf{m} \end{bmatrix} = \begin{bmatrix} \mathbf{D}_x \\ \mathbf{D}_y \\ \mathbf{D}_z \end{bmatrix} \mathbf{m}, \quad (43)$$

where \mathbf{D}_x , \mathbf{D}_y , and \mathbf{D}_z are global matrices of $(\mathbf{D}_x)_{c_0}$, $(\mathbf{D}_y)_{c_0}$, and $(\mathbf{D}_z)_{c_0}$. For a given mesh, the square matrices \mathbf{D}_x , \mathbf{D}_y , and \mathbf{D}_z are computed once and reused in the joint inversion. The cost to build and store the matrices \mathbf{D}_x , \mathbf{D}_y , and \mathbf{D}_z are cheap. First, the operation counts to construct \mathbf{D}_x , \mathbf{D}_y , and \mathbf{D}_z are proportional to the number of elements of the mesh, which is fast in terms of floating-point operations. Second, \mathbf{D}_x , \mathbf{D}_y , and \mathbf{D}_z are sparse with only five nonzero entries per row (one for the element itself and the rest for its four neighbors), which is efficient in terms of memory storage. Also, operations involving \mathbf{D}_x , \mathbf{D}_y , and \mathbf{D}_z can be executed quickly using the element sparse operations. The above formulas can be extended to the gradient calculation for arbitrary polyhedron by adjusting the number of neighboring cells.

3.0 Parallel Implementation

E4D (Johnson et al. 2010; Johnson and Wellman 2015) is a parallel 3D finite element modeling and inversion code for subsurface imaging and monitoring using static and time-lapse DC resistivity data. To address the computational demands of inverting large-scale 3D (either static or time-lapse) data sets, E4D runs on high-performance computing systems with distributed memory. E4D also supports modeling and inversion of traveltimes data using the fast marching method (Lelièvre et al. 2011).

We developed a new E4D module for structural-coupled joint inversion of DC resistivity and traveltimes data. This joint inversion module utilizes existing E4D parallel computations for single geophysical methods, including forward simulation, distributed storage and computation of the Jacobian matrix of forward operator, and parallel execution of matrix-vector multiplication during inversion (Johnson et al., 2010). Besides, the joint inversion is divided into two parallel NLCG processes, one for DC resistivity and the other for traveltimes data, each with its own master and slave processors (Figure 1).

The NLCG parallel process stores observed and predicted data, model parameters, Jacobian matrix of forward operator, data and model weightings for each physics on the designated master processor. In the outer loop of NLCG, the two master processors compute predicted data and Jacobian matrix independently in parallel and exchange the model parameters of different physics to construct the Jacobian matrix of cross-gradient operator. In the inner loop of NLCG, the master processors run the PCG algorithm for the two physics in parallel and communicate with each other for the step length and coefficient of the conjugate direction in each inner iteration (Figure 1).

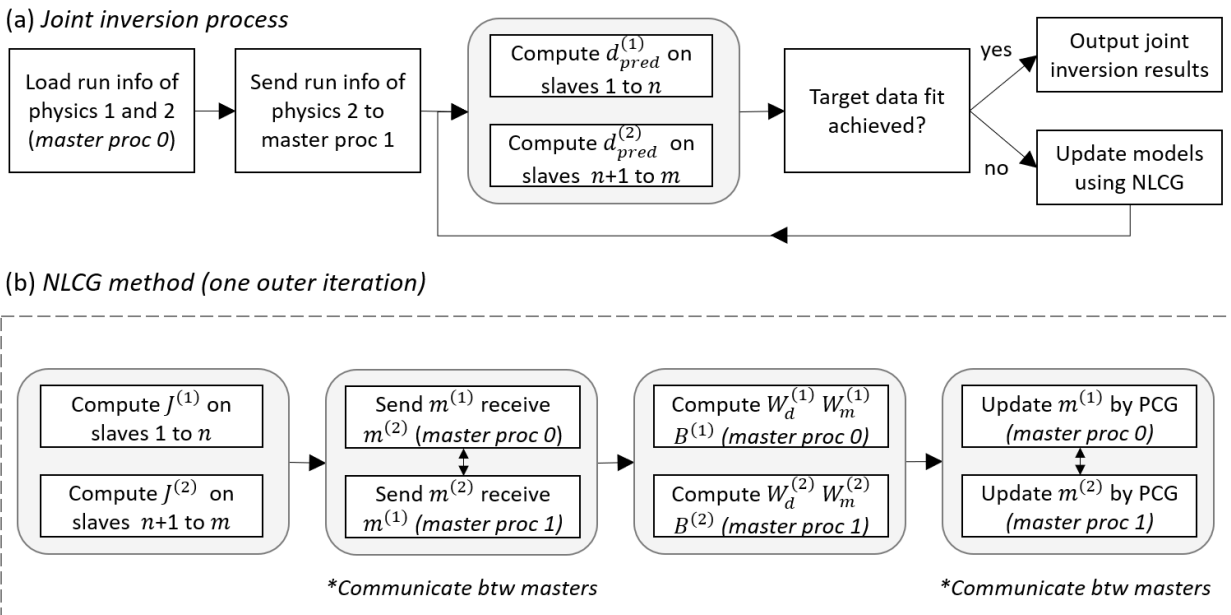


Figure 1. Generalized flow diagram demonstrating the (a) joint inversion process and (b) NLCG method. Gray box shows parallel tasks distributed among masters or slaves. Parallel computations of the forward simulation and Jacobian of the forward operator are distributed evenly among slaves and details can be found in Johnson et al. (2010).

The NLCG process runs in parallel between the two groups (Figure 1b). In one outer iteration of NLCG, the two groups compute Jacobian in dependently and simultaneously. After the Jacobian computations, the master nodes of the two groups exchange the current model parameters and compute data weighting, model weighting, and cross-gradient **B** matrices for the assigned physics. In the last step of one NLCG

outer iteration, the two master processors update the model parameters using the PCG algorithm in parallel. During this model update, the two master processors communicate the step length and conjugate direction. The NLCG process is repeated until the data are appropriately fit (Figure 1a.)

4.0 Synthetic Study

4.1 Synthetic Model Setup

The synthetic model consists of two rectangular anomalies, each of size 8 m x 8 m x 5 m, buried in a homogeneous half-space as shown in Figure 2a. One of the anomalies had larger conductivity and lower velocity and the other had smaller conductivity and higher velocity than the surroundings. The conductivity and velocity of the two anomalies and surrounding half-space are given in Figure 2b.

Computational mesh for the DC resistivity and traveltimes modeling and inversion were the same, with central part shown in Figure 2a. The entire mesh extended to a much larger volume (1000 m x 1000 m x 500 m) than the observation domain to reduce the boundary effects in the DC resistivity modeling. The mesh was refined near electrode locations to accommodate large potential gradients nears sources and sinks. The mesh contained 164,672 tetrahedral elements in total.

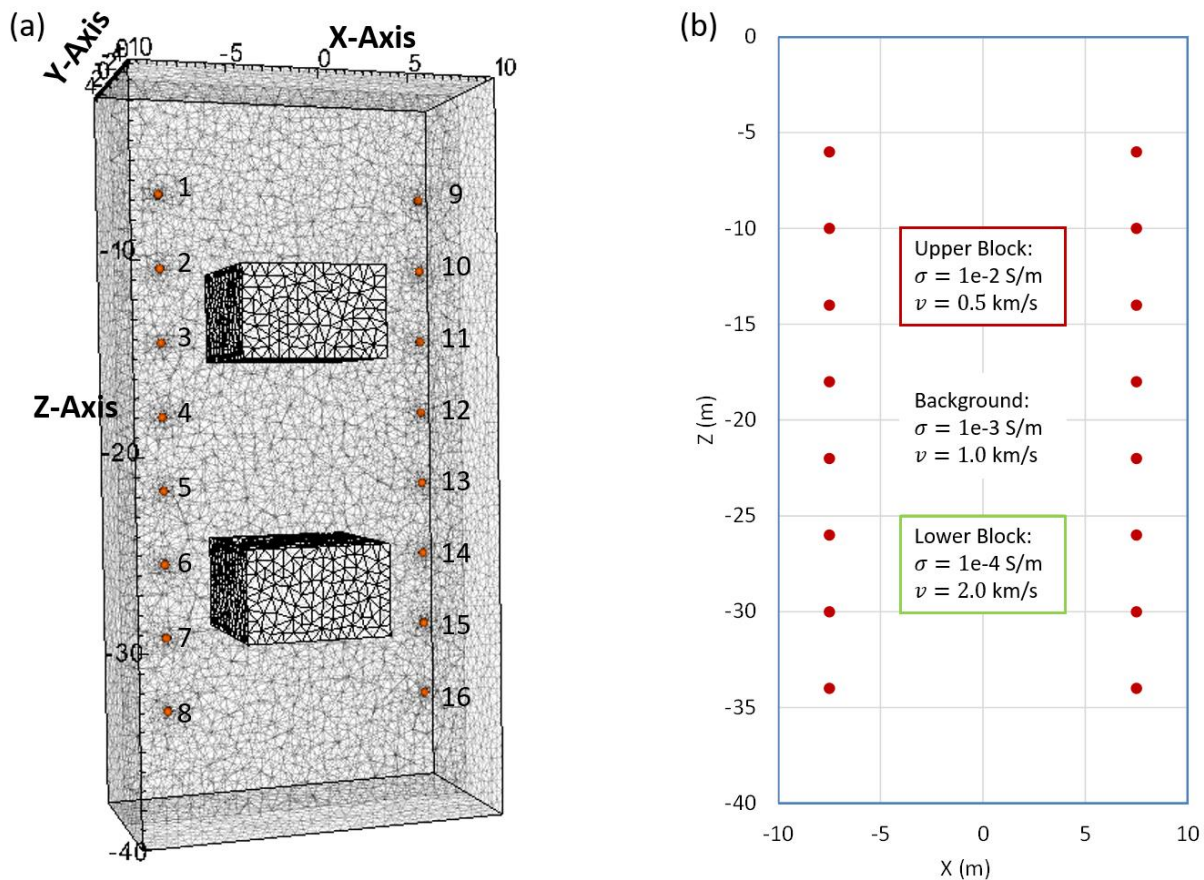


Figure 2. Central computational domain and electrode positions. The traveltimes receivers and transmitters are co-located with the electrodes. (a) Geometry of the two 8 m x 8 m x 5 m blocks. (b) Conductivity and velocity of the two blocks and surrounding area.

Synthetic DC resistivity and traveltimes surveys were conducted along two vertical boreholes that were 15 m apart. Each borehole had 8 electrodes (16 in total) evenly spaced between $z = -6$ and $z = -34$ m. Two consecutive electrodes were used as current source and sink (i.e. electrodes A and B) and another two consecutive electrodes (i.e. electrodes M and N) were used to measure the potential difference. A total of 79 transfer resistance data were collected for such a DC resistivity survey configuration.

Traveltime sources/receivers were co-located at the positions of the borehole electrodes. With 8 sources in one borehole and 8 receivers in the other, a total of 64 traveltimes were collected.

4.2 Separate and Joint Inversion Results

The synthetic DC resistivity and traveltimes data were inverted separately and jointly for logarithmic of conductivity $\log(\sigma)$ and slowness s (reciprocal of velocity). That is,

$$m^{(1)} = \log \sigma, m^{(2)} = s.$$

Each element in the modeling mesh was used as an inversion parameter characterized by $m^{(1)}$ and $m^{(2)}$. We recommend using initial conductivity and velocity values close to the solutions of the separate inversions to overcome local minima associated with the nonlinearity of the cross-gradient function.

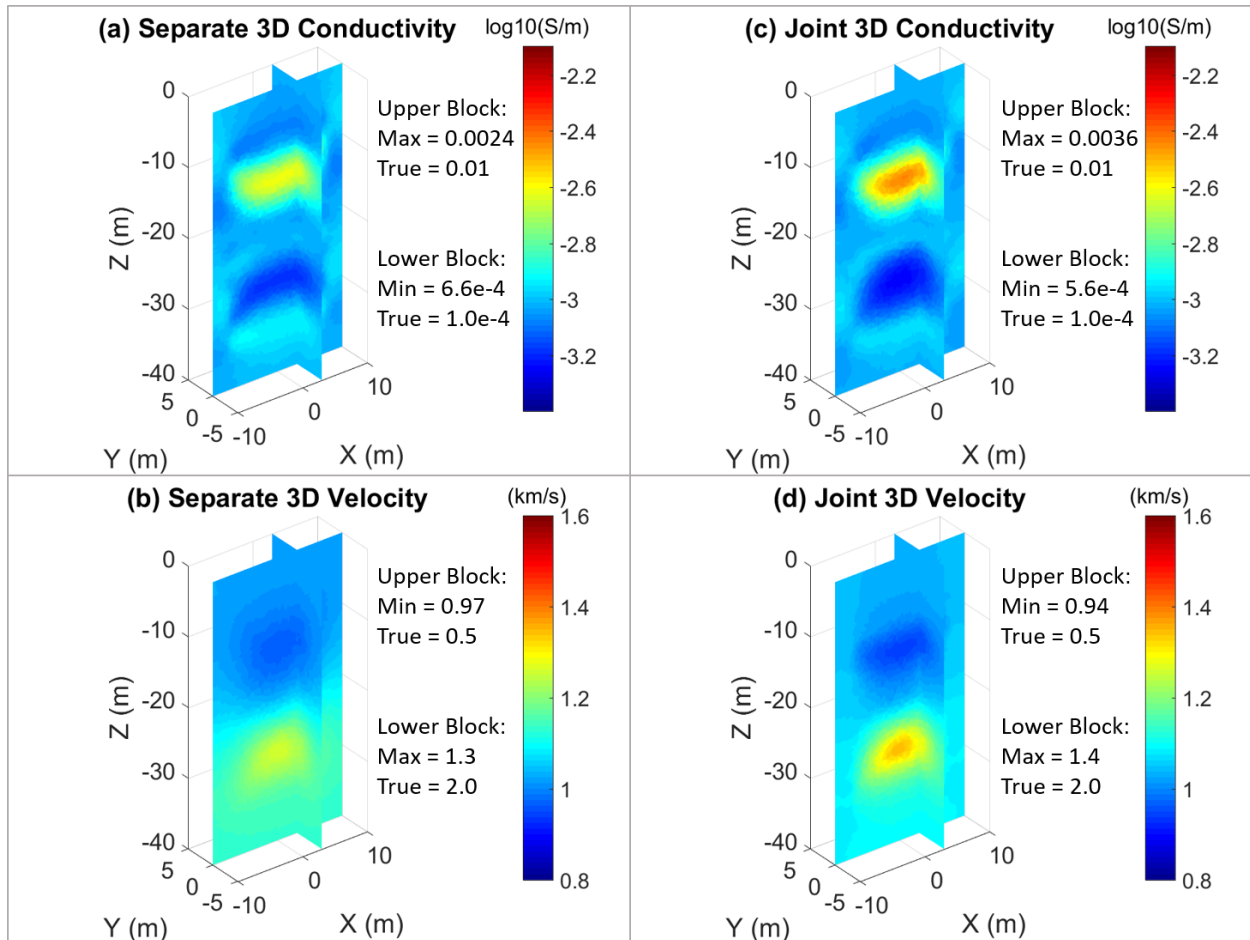


Figure 3. Conductivity and velocity recovered from the separate and joint inversions. (a) Conductivity from the separate inversions. (b) Velocity from the separate inversions. (c) Conductivity from the joint inversion. (d) Velocity from the joint inversion.

The synthetic DC resistivity and traveltimes data were jointly inverted using exact \mathbf{H} matrix in Eq. **Error! Reference source not found.** and initial models close to the separate inversion results. Figure 3 shows the spatial distribution of the conductivity and velocity from the separate and joint inversions. For this synthetic case, either the separate inversion of conductivity or velocity or the joint inversion of both

produced reasonable results. Both the upper and lower blocks were clearly identified. This means that either of the datasets is sufficient to identify the two anomalies in the subsurface.

However, there are some differences between the inverted results from separate and joint inversions. For all cases, if the property value of an anomaly was higher than that of the surrounding area, the property value was underestimated by all the inversions, but at a relatively less magnitude by the joint inversion than the separate inversions. For example, the upper block had the true conductivity of 0.01 S/m. The maximum value was 0.0024 S/m from the separate inversion (Figure 3a) and was 0.0036 S/m from the joint inversion (Figure 3c). Vice versa, if the property value of an anomaly was lower than that of the surrounding area, the value was overestimated, but again at a relatively less magnitude by the joint inversion than separate inversion. For example, the upper block had the true velocity of 0.5 km/s. The minimum value was 0.97 km/s from the separate inversion (Figure 3b) and 0.94 km/s from the joint inversion (Figure 3d). These results indicate that the results from joint inversion gave a stronger signal of the existence of the anomalies than those from separate inversions.

Figure 4 shows the shape and size of the identified anomalies with the background values blanked off. Because of the different sensitivity of different geophysical methods, by comparing Figure 4a and Figure 4c, it can be clearly seen that the shape and size of the identified anomalies were different from the two separate inversions. The discrepancy in shape and size of anomalies created a problem because the results do not tell which one is more reliable. In contrast to the separate inversions, the shape and size of the anomalies from the joint inversion, which imposed structural similarities between $\log(\sigma)$ and s , were relatively similar (Figure 4b and Figure 4d). These results indicate that the shape and size of the anomalies from the joint inversion are more reliable than those from the separate inversions.

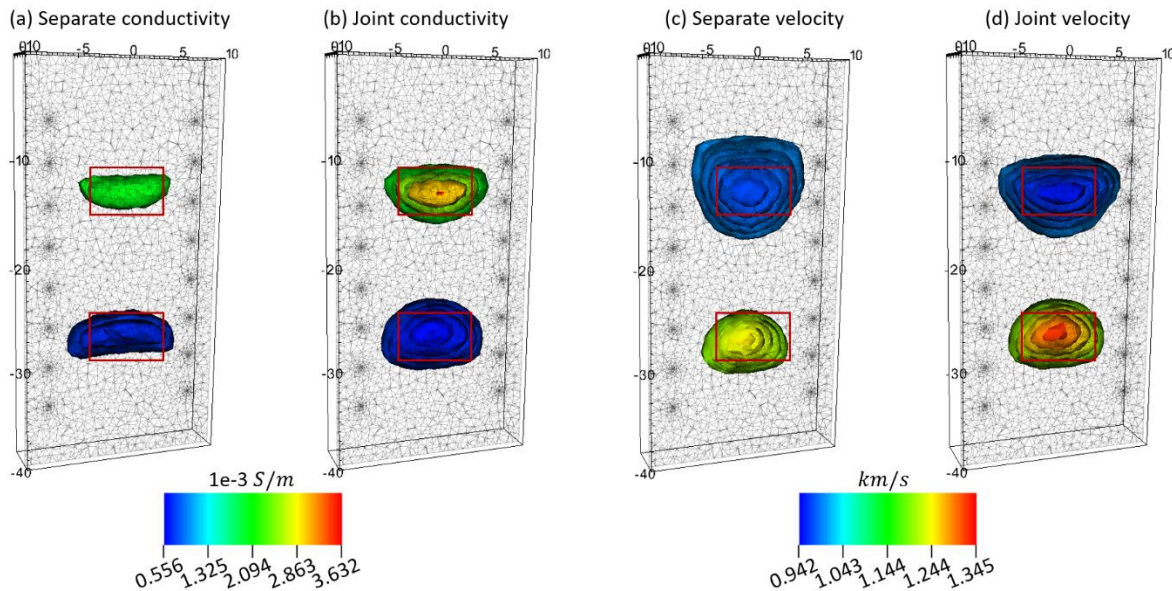


Figure 4. Cut-off plots of the recovered anomalies with background blanked off. The red rectangles indicate the true size and location of the two blocks. The shape and size of the anomalous conductivity and velocity are more correlated in the joint inversion results.

4.3 Relationships Between Conductivity and Velocity

The properties of subsurface anomalies are often correlated but the correlation relationship may be different for different anomalies. These relationships can be shown by cross plots of conductivity versus slowness (Figure 5). The two separate inversions were conducted without imposing any correlation, the

correlation levels were relatively low (Figure 5a). During the joint inversion, the correlation between the two properties was enforced, as expressed by the cross-gradient function in Eq. (2). As a result, the correlation between the two properties was considerably improved (Figure 5b). For the upper anomaly, R^2 increased from 0.598 of the separate inversion to 0.894 of joint inversion. For the lower anomaly, R^2 increased from 0.399 of the separate inversion to 0.876 of joint inversion. The improvement of R^2 indicates that joint inversion can better distinguish different anomalies in the subsurface.

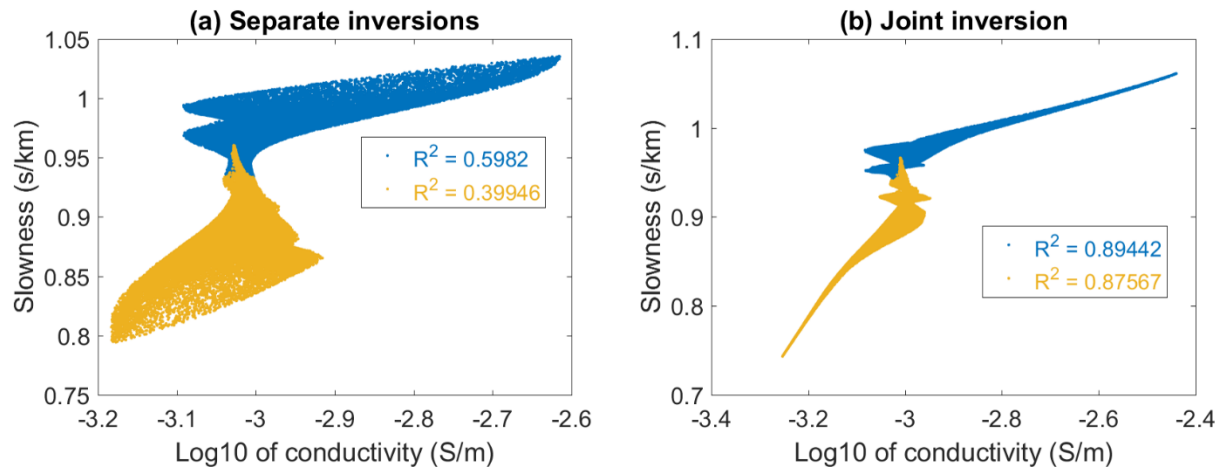


Figure 5. Cross plots of conductivity versus slowness (reverse of velocity) derived from the (a) separate and (b) joint inversions. Each dot represents an inversion element characterized by conductivity (x-axis) and slowness (y-axis). The blue and yellow dots represent the upper and lower anomalies and their surround areas, respectively.

5.0 Conclusions

We have presented a parallel distributed-memory joint inversion code for DC resistivity and traveltimes data on unstructured mesh. The code inherits the parallel framework of E4D and is suitable for large scale 3D subsurface characterization for multi-physics data. (how and when different physics communicate with each other.) We have demonstrated through a synthetic cross-borehole model that the shape and size of the anomalies from the joint inversion are more reliable than those from the separate inversions. The joint inversion detected smaller property contrast in the conductivity and velocity models. The cross-gradient constraint in the joint inversion enforced element-to-element structural coupling and thus allowed to recover anomalies characterized by nonuniform relationships between the different physical properties (i.e. multiple slopes in the cross plots).

6.0 References

- Ascher UM and C Greif. 2011. *A First Course in Numerical Methods*. Society for Industrial and Applied Mathematics.
- Calamita G, A Perrone, L Brocca, B Onorati, and S Manfreda. 2015. "Field Test of a Multi-Frequency Electromagnetic Induction Sensor for Soil Moisture Monitoring in Southern Italy Test Sites," *Journal of Hydrology*, 529:316-329. doi:<https://doi.org/10.1016/j.jhydrol.2015.07.023>.
- Colombo D and MD Stefano. 2007. "Geophysical Modeling Via Simultaneous Joint Inversion of Seismic, Gravity, and Electromagnetic Data: Application to Prestack Depth Imaging," *The Leading Edge*, 26(3):326-331. doi:10.1190/1.2715057.
- Doolittle JA and EC Brevik. 2014. "The Use of Electromagnetic Induction Techniques in Soils Studies," *Geoderma*, 223-225:33-45. doi:<https://doi.org/10.1016/j.geoderma.2014.01.027>.
- Gallardo LA and MA Meju. 2004. "Joint Two-Dimensional DC Resistivity and Seismic Travel Time Inversion with Cross-Gradients Constraints," *Journal of Geophysical Research: Solid Earth*, 109(B3). doi:10.1029/2003jb002716.
- Haber E and D Oldenburg. 1997. "Joint Inversion: A Structural Approach," *Inverse Problems*, 13(1):63-77. doi:10.1088/0266-5611/13/1/006.
- Jegen MD, RW Hobbs, P Tarits, and A Chave. 2009. "Joint Inversion of Marine Magnetotelluric and Gravity Data Incorporating Seismic Constraints: Preliminary Results of Sub-Basalt Imaging Off the Faroe Shelf," *Earth and Planetary Science Letters*, 282(1):47-55. doi:<https://doi.org/10.1016/j.epsl.2009.02.018>.
- Johnson TC. 2014. *E4D: A Distributed Memory Parallel Electrical Geophysical Modeling and Inversion Code*, PNNL-SA-23783, Pacific Northwest National Laboratory. Richland, Washington. Available at <https://e4d.pnnl.gov/Pages/Home.aspx> (Accessed on June 14, 2016).
- Johnson TC, R Versteeg, A Ward, F Day-Lewis, and A Revil. 2010. "Improved Hydrogeophysical Characterization and Monitoring through Parallel Modeling and Inversion of Time-Domain Resistivity And induced-Polarization Data," *Geophysics*, 75(4):WA27-WA41. doi:10.1190/1.3475513.
- Johnson TC and D Wellman. 2015. "Accurate Modelling and Inversion of Electrical Resistivity Data in the Presence of Metallic Infrastructure with Known Location and Dimension," *Geophysical Journal International*, 202(2):1096-1108. doi:10.1093/gji/ggv206.
- Lavoué F, J Van Der Krak, J Rings, F André, D Moghadas, JA Huisman, S Lambot, L Weiherrnüller, J Vanderborght, and H Vereecken. 2010. "Electromagnetic Induction Calibration Using Apparent Electrical Conductivity Modelling Based on Electrical Resistivity Tomography," *Near Surface Geophysics*, 8(6):553-561. doi:10.3997/1873-0604.2010037.
- Lelièvre PG, CG Farquharson, and CA Hurich. 2011. "Computing First-Arrival Seismic Traveltimes on Unstructured 3-D Tetrahedral Grids Using the Fast Marching Method," *Geophysical Journal International*, 184(2):885-896. doi:10.1111/j.1365-246X.2010.04880.x.

- Martínez G, K Vanderlinden, JV Giráldez, AJ Espejo, and JL Muriel. 2010. "Field-Scale Soil Moisture Pattern Mapping Using Electromagnetic Induction," *Vadose Zone Journal*, 9(4):871-881. doi:10.2136/vzj2009.0160.
- Martini E, U Werban, S Zacharias, M Pohle, P Dietrich, and U Wollschläger. 2017. "Repeated Electromagnetic Induction Measurements for Mapping Soil Moisture at the Field Scale: Validation with Data from a Wireless Soil Moisture Monitoring Network," *Hydrol. Earth Syst. Sci.*, 21(1):495-513. doi:10.5194/hess-21-495-2017.
- Meju MA, RL Mackie, F Miorelli, AS Saleh, and RV Miller. 2019. "Structurally Tailored 3d Anisotropic Controlled-Source Electromagnetic Resistivity Inversion with Cross-Gradient Criterion and Simultaneous Model Calibration," *GEOPHYSICS*, 84(6):E387-E402. doi:10.1190/geo2018-0639.1.
- Molodtsov DM, VN Troyan, YV Roslov, and A Zerilli. 2013. "Joint Inversion of Seismic Traveltimes and Magnetotelluric Data with a Directed Structural Constraint," *Geophysical Prospecting*, 61(6):1218-1228. doi:10.1111/1365-2478.12060.
- Moorkamp M, B Heincke, M Jegen, AW Roberts, and RW Hobbs. 2011. "A Framework for 3-D Joint Inversion of Mt, Gravity and Seismic Refraction Data," *Geophysical Journal International*, 184(1):477-493. doi:10.1111/j.1365-246X.2010.04856.x.
- Shewchuk JR. 1994. *An Introduction to the Conjugate Gradient Method That Even an Idiot Can Understand*. Pittsburgh, Pa. : School of Computer Science, Carnegie Mellon University, [1994].
- Zhdanov MS, A Gribenko, and G Wilson. 2012. "Generalized Joint Inversion of Multimodal Geophysical Data Using Gramian Constraints," *Geophysical Research Letters*, 39(9). doi:10.1029/2012gl051233.

Pacific Northwest National Laboratory

902 Battelle Boulevard

P.O. Box 999

Richland, WA 99354

1-888-375-PNNL (7665)

www.pnnl.gov